Thermal-hydraulic performance of discontinuous fin heat exchanger geometries using Supercritical CO$_2$ as the working fluid

Sandeep R Pidaparti
Graduate Research Assistant
Georgia Institute of Technology
Atlanta, GA 30318

Mark Anderson
Research Professor
University of Wisconsin – Madison
Madison, WI 53706

Devesh Ranjan
Associate Professor
Georgia Institute of Technology
Atlanta, GA 30318

ABSTRACT

The supercritical carbon dioxide (sCO$_2$) Brayton cycles have the potential to attain higher cycle efficiencies that the conventional steam Rankine cycles and air Brayton cycles. This is primarily achieved by lowering the power required to compress CO$_2$ near its critical point and by using a high degree of thermal recuperation. Using compact exchangers (Such as the diffusion-bonded heat exchangers) for thermal recuperation would lead to cost-effective, simpler and compact cycle footprint. Commercially available diffusion-bonded heat exchangers comprises set of continuous zigzag channels to enhance the heat transfer. Such PCHEs can suffer from excessive pressure drop and flow maldistribution which has a direct negative impact on the sCO$_2$ Brayton cycle efficiency. Current study focuses on the experimental thermal-hydraulic performance evaluation of the discontinuous offset rectangular and airfoil fin surface patterns. These surface patterns are etched on to type 316 stainless steel plates using photo-chemical etching technology, emulating techniques used to manufacture commercial PCHEs. Local and average heat transfer coefficients and average friction factors were measured over a wide range of operating conditions relevant to the supercritical CO$_2$ Brayton cycles. The discontinuous offset rectangular and airfoil fin plates exhibited significantly lower pressure drop compared to the commercial continuous zig-zag channel PCHEs.

INTRODUCTION

The supercritical carbon dioxide (sCO$_2$) Brayton cycle is an attractive heat-to-power conversion option for the next generation nuclear, concentrated solar and fossil-fired power plants. The sCO$_2$ Brayton cycle offers higher thermodynamic efficiency within a compact foot print compared to superheated/supercritical steam Rankine or air Brayton cycles in the temperature range of interest for these power plants. The cycle combines the inherent advantages of the steam Rankine cycle (small back work ratio) and the ideal gas Brayton cycle (single phase fluid) by utilizing CO$_2$ above its critical pressure and temperature. To achieve the high cycle thermal efficiencies, the sCO$_2$ Brayton cycle requires significant amount of internal heat recuperation thus requiring numerous, large heat exchangers. Consequently, the total capital cost of the power block is dominated by the capital cost of the heat exchangers. An effective way to handle high operating pressures, temperatures as well as to reduce the capital cost is to use compact heat exchangers for the sCO$_2$ Brayton cycle. Compact diffusion bonded heat exchangers, such as PCHEs marketed by Heatric, are the leading heat exchanger candidates for the sCO$_2$ Brayton cycles. A PCHE can be considered as a branch of the plate-fin type heat exchanger family and rely mainly on the two unconventional technologies of photo-chemical etching and diffusion bonding. In the first step, desired flow channels/patterns are chemically etched on to flat metal plates. The etched plates are then stacked and diffusion bonded to form PCHE core. The main advantage of PCHEs is that they allow for etching a wide range of surfaces thus altering the thermal-hydraulic performance of the PCHE core quite easily without adding much to their capital cost. Although PCHEs have been around for

a while mainly in the oil & gas industry, their use in the power generation industry gained popularity about a decade ago. Since then decent number of experimental and computational studies have been published in literature to understand the thermal-hydraulic performance of different PCHE surface geometries using mainly Carbon dioxide, air, water or Helium as the working fluid. Most of the studies in the literature are focused on either experimental or numerical investigations into either continuous zigzag style or straight channels which are commercially available through Heatric or custom fabricated. What follows is a brief compilation of testing and numerical modeling efforts undertaken by different research groups from the literature.

Based on the literature review, the surface geometries of PCHEs can be categorized as either continuous or discontinuous fin surfaces. Continuous fin surfaces include straight, sinusoidal, and zig-zag channels, while discontinuous fin surfaces include louver, S-shaped, and airfoil geometries. Some of the earliest work on PCHEs was performed at Tokyo Institute of Technology [1]-[7]. They tested a zig-zag channel Heatric PCHE for CO_2-to-CO_2 service and proposed empirical correlations for the effective friction factor and the local heat transfer coefficients using Fluent[TM] [1, 2]. Tsuzuki et al. [3] conducted CFD studies and concluded that the surface geometry with S-shaped fins, similar to that of a sine curve offered a significantly lower pressure drop compared to the zig-zag channel. The S-shaped fins offered a more uniform velocity profile and eliminated the swirl flows, eddies, and recirculation zones experienced by continuous zig-zag channels. Kato [4] showed the S-shaped fin geometry attained about six times lower pressure drop relative to the continuous zig-zag channel while maintaining nearly similar heat transfer performance. Ngo et al. [5] fabricated a new PCHE with S-shaped fins and tested it for CO_2-to-water service. Nikitin et al. [6] experimentally evaluated the thermal-hydraulic performance of PCHE with S-shaped fins and a conventional PCHE with zig-zag channels. It was concluded that the pressure drop of PCHE with S-shaped fins is 4-5 times lower than that of PCHE with zig-zag channels but at the same time Nusselt number is 24-34% lower depending on the Reynolds number. Ngo et al. [7] extended the range of operating conditions for both the PCHEs and proposed Nusselt number and friction factor empirical correlations for S-shaped fins and zig-zag channel PCHEs. Moisseytsev et al. [8] tested a 17.5 kW$_{th}$ 316L stainless steel Heatric PCHE for conditions relevant to the low temperature recuperator of the sCO$_2$ Brayton cycle. Using the published sample friction factor and colburn j-factor for Heatric PCHEs [9], Moisseytsev et al. [8] performed curve fits and proposed friction factor and j-factor correlations as shown in Equations (1)-(3).

The friction factor for straight channels (referred to as "plain") is calculated as shown in Equation (1),

$$f_0 = \begin{cases} \frac{16}{Re}, & Re < 1700 \\ \frac{0.0791}{Re^{0.25}}, & Re > 2300 \end{cases} \tag{1}$$

With a linear function for the transition region (1700 < Re < 2300).
The zig-zag channel friction-factor enhancement is calculated using the form of Equation (2),

$$\frac{f}{f_0} = \begin{cases} 1 + a_f(Re + 50), & Re < 1300 \\ kRe^c, & Re \geq 1300 \end{cases} \tag{2}$$

Where,

$$c = \frac{\ln\frac{1+223283.a_f^2}{1+a_f.1800}}{\ln\left(\frac{1000}{13}\right)}$$

$$k = \frac{1+a_f.1800}{1300^c}$$

$$a_f = 4.5 \cdot 10^{-3} \tan\theta_b$$

The j-factor correlations were developed separately for the laminar and turbulent regions as presented in Equation (3).

$$j = \begin{cases} \frac{4.1}{Re}(1 + a_{j,lam}(Re + 50)), & Re < 2300 \\ a_{j,turb}(0.1341)Re^{-0.3319}, & Re \geq 2300 \end{cases} \tag{3}$$

Where the coefficients are defined as follows,

$$a_{j,turb} = 0.6 + 0.5\tan\theta_b$$
$$a_{j,lam} = \frac{3.9361 \cdot a_{j,turb} - 1}{1800}$$

It was found that the following fit provides better heat transfer prediction for the straight channel in the transition region. As such, no special treatment is necessary for the zig-zag channels.

$$j_{0,trans} = 352 Re^{-1.4562}$$

Kim *et al.* [10-12] tested an Alloy 800H Heatric PCHE for conditions relevant to the High temperature gas cooled reactors (HGTRs). They conducted a series of tests for He-to-He, He-to-water, and He+CO_2 mixture-to-water service and proposed global and local averaged friction factor and Nusselt number correlations. Mylavarapu et al. [13] tested two Alloy 617 custom fabricated PCHEs with semi-circular straight channels for conditions relevant to Very high temperature gas reactors (VHTR). They compared the experimentally determined friction factor and Nusselt numbers to the fully developed, constant-property smooth circular pipe correlations for turbulent and laminar-to-turbulent transition flow regimes. Mylavarapu *et al.* [13] data suggested that in the case of semi-circular channel, the laminar-to-turbulent flow transition occurred at *Re* of approximately 1700; earlier than *Re* of 2300 for circular channel. This expedited transition is attributed to the rough inlet at the entrance to the PCHE. Kruizenga *et al.* [14] and Carlson [15] tested straight, zig-zag channels, and discontinuous NACA0020 airfoil fin geometries and compared their thermal-hydraulic performance. The idea of utilizing NACA0020 airfoil fin geometries for PCHEs seem to be motivated by the CFD study conducted by Kim *et al.* [16]. Kim *et al.* [16] study showed that the airfoil fin yielded the same heat transfer performance as the zig-zag channel but at a significantly lower pressure drop (~1/20) due to the suppression of separated flows. Although not as dramatic as shown by the CFD study, Carlson [15] experiments indeed indicated that the airfoil fin geometries offer significantly lower pressure (almost equal to that of roughened circular tubes with equivalent hydraulic diameter). However, most of these experiments were conducted near the pseudo-critical point ($T_b/T_{pc} < 1.2$), where the heat transfer is significantly influenced by the thermo-physical property variations rather than the geometrical parameters. This warrants additional investigation into the discontinuous airfoil fin geometries for the diffusion bonded heat exchangers. This work aims at experimental evaluation of the thermal-hydraulic performance of discontinuous rectangular and NACA0020 airfoil fin geometries.

EXPERIMENTAL TEST FACILITY AND DATA REDUCTION

Figure 1 shows the picture of the test rig utilized for the current work. The test loop consists of high pressure liquid chromatography (HPLC) pump, circulation gear pump, Coriolis mass flowmeter, pre-heater, test section and an after-cooler. Prior to the beginning of testing, the test loop is vacuumed and purged with CO_2 to ensure that no foreign contaminants are present in the system. The facility is filled with CO_2 up to desired operating pressures using Scientific Systems, Inc. SFC-24 positive displacement, constant pressure HPLC pump. Once the test loop is at desired operating pressures, Micropump magnetically driven gear pump is used to circulate the fluid in the loop. The pump is coupled to a variable frequency drive (VFD); this in conjunction with a flow bypass valve adjusts and precisely controls the desired mass flowrate through the heat exchanger. A Micromotion Coriolis mass flowmeter and transmitter are used to record the mass flowrate through the test section as well as to provide the feedback to the circulation pump via VFD. The temperature of fluid entering the test section is controlled using a custom fabricated 5.5 kW high pressure cartridge heater. More details of the test facility can be found from Pidaparti *et al.* [17]. The prototypic discontinuous heat exchanger patterns for this work are tested in the same manner as Kruizenga *et al.* [14] and Carlson [15]. The model and sketch of the heat exchanger shown in Figure 2 is a good representation of the heat exchanger, fluid paths, and the instrumentation.
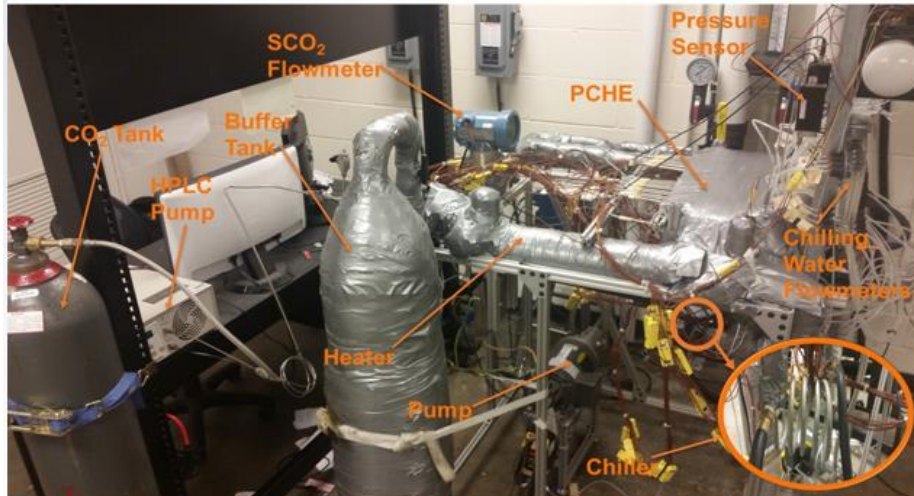
Figure 1: Picture of the sCO$_2$ heat exchanger test facility at Georgia Tech.

The test section comprises of the heat exchanger plate, the mating plate, and the cooling blocks. This design allows for multiple heat exchanger patterns to be tested by swapping out the heat exchanger plates whenever necessary. For this work we tested two different heat exchanger plates (discontinuous rectangular offset fin and NACA0020 airfoil fin geometries). The heat exchanger plate is a 316L stainless steel plate with the desired pattern chemically etched on to it and the total length of the etched pattern is 500 mm. On each end of the plate, entrance and exit manifolds are machined into the plate to distribute and collect the flow entering and leaving the test section. Figure 3 shows a section of the two discontinuous fin geometries tested for the current work and their corresponding representative unit cell geometry.
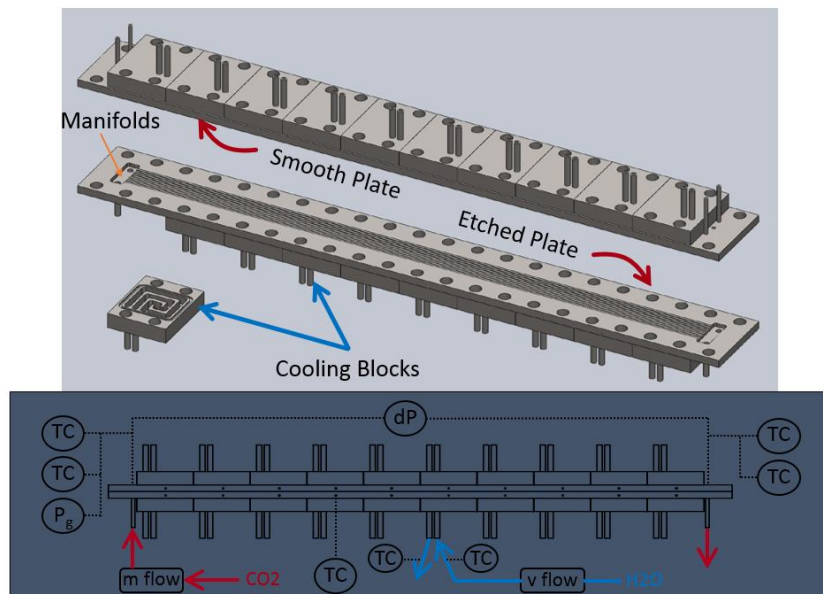

Figure 2: CAD model and Sketch of the heat exchanger showing assembly, fluid paths, and the instrumentation [15].

To verify the dimensions of the surface geometrical patterns the plates are scanned by Laser Design, Inc. under a laser scanner with a scan resolution of 0.0127 mm. The .stl file generated from this process was analyzed to measure the various geometrical features. Table 1 and Table 2 presents the designed and measured surface geometry features for the offset rectangular and NACA0020airfoil fin geometries respectively.

Two RTDs are located in each manifold to measure the inlet and outlet temperatures of the CO_2. The inlet pressure and the differential pressure across the test section are measured using a Meriam ZM1500-GI3000 and ZM1500-DN0415 digital transmitters respectively. The heat exchanger plate is bolted to the mating plate to complete the prototypic heat exchanger emulating the diffusion bonded heat exchangers. The mating plate is essentially a flat plate with an O-ring groove machined into the surface, along with three holes at each end, two for thermocouples and one for a pressure tap. The O-ring is used to seal the heat exchanger and is made of 1/16" Viton cord stock and that is cut to the length and glued together to form the seal. One of the objective of these tests is to measure local heat transfer coefficients. In order to achieve this, local heat fluxes, wall temperatures and fluid bulk temperatures need to be accurately determined.
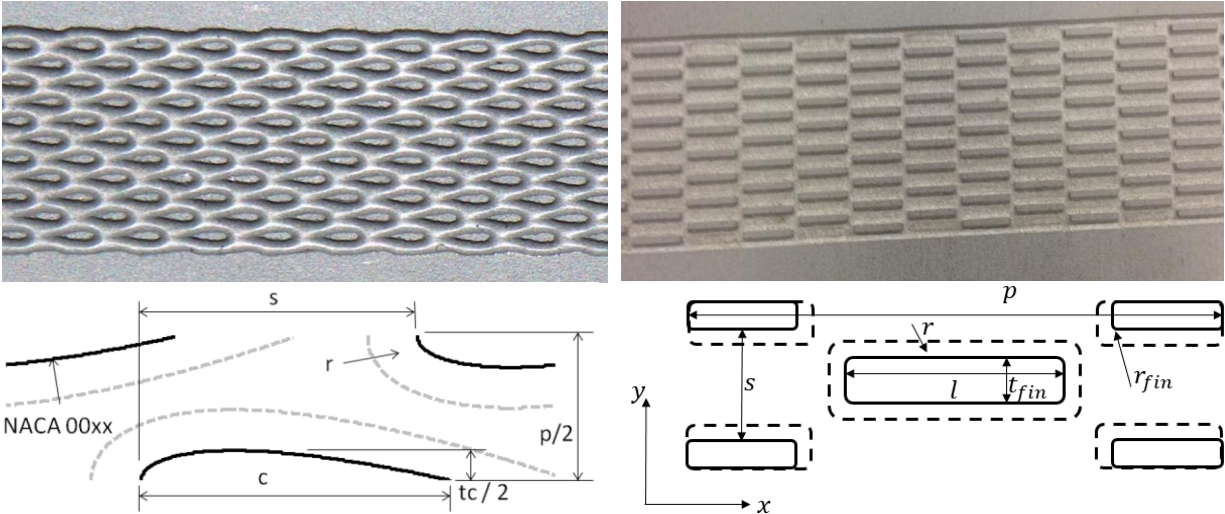

Figure 3: Images representing a section of the NACA0020 airfoil fin (Top Left) and rectangular Offset fin (Top Right) geometry heat exchanger plates. Unit cell representation of NACA0020 airfoil fin (Bottom Left) and rectangular offset fin (Bottom Right).

Table 1: Design and measured geometrical parameters of the Offset rectangular fin pattern (Refer to Figure 3 for the nomenclature)

	Design	Measured
Fin thickness, t_{fin} (mm)	0.65	0.65
Fillet radius, r (mm)	0	0.47
Fillet radius, r_{fin} (mm)	0	0.18
Fin depth, h (mm)	0.65	0.65
Fin spacing, s (mm)	1.95	1.95
Fin length, l (mm)	9.025	7.69
Lateral pitch, p (mm)	18.05	17.68
Plate thickness, t (mm)	6.3	
Number of unit cells along length (N_x)	28	
Number of unit cells per row (N_y)	9	
Hydraulic diameter, D_h (mm)	0.9502	0.9973
Unit cell heat transfer area, A_s (mm^2)	82.01	91.133
Cross-sectional area, A_c (mm^2)	11.43	11.567
Measured Relative roughness	7.4e-3	

Table 2: Design and measured geometrical parameters of the Offset NACA0020 Airfoil fin pattern (Refer to Figure 3 for the nomenclature)

	Design	Measured
Chord width, c (mm)	4	3.566
Thickness/Chord length	0.2	0.202
Fillet radius, r (mm)	0	0.795
Channel depth, h (mm)	0.95	0.685
Axial pitch, s (mm)	3.5	3.466
Lateral pitch, p (mm)	3.6	3.657
Plate thickness, t (mm)	6.3	
Number of Rows (N_x)	144	
Airfoils per Row (N_y)	6	
Hydraulic diameter, D_h (mm)	1.205	1.112
Unit cell heat transfer area, A_s (mm^2)	30.18	24.94
Cross-sectional area, A_c (mm^2)	15.96	12.07
Measured Relative roughness	7.259e-3	

In order to measure local wall temperatures, a set of ten 1/16" thermocouples are implanted into the side wall of each plate. Thermocouples are thermally coupled to the wall and the holes are filled using excess thermal paste which has excellent thermal conductivity and allows for easy cleaning and replacement of thermocouples when needed. This step was necessary to avoid any temperature gradients induced due to the presence of air pockets that could lead to several degrees of error in wall temperature measurement. Attached to the top of the mating plate and bottom of the heat exchanger plate are a set of ten individual cooling blocks that are used to measure local heat removal rate. Each cooling block is supplied with cooling water. Volumetric flowrate of water flowing to each cooling block is measured using turbine type flowmeters. Two K-type thermocouples are installed into the water at the inlet and outlet of each cooling block to measure the temperature of water entering and leaving the cooling block, refer to Figure 2.

Experimental conditions

The experiments were conducted for both the heat exchanger plates presented above for a wide range of operating conditions relevant to the sCO$_2$ Brayton cycles and are described in Table 3. These conditions provided a wide range of average Re, 2700 < Re < 38,000 and average Pr, 0.8 < Pr < 25. A total of 453 and 306 experiments were performed for each of the Offset rectangular and NACA0020 Airfoil fin geometries respectively.

Table 3: Range of experimental conditions for both the heat exchanger plates

Inlet pressure (MPa)	7.5, 8.1, 10.2
CO$_2$ Inlet temperature (^{o}C)	50 – 200°C (In increments of 10°C) 20 – 50°C (In increments of 5°C)
CO$_2$ flow rate (kg/h)	8.8 – 28.8 kg/h (In increments of 2.9 kg/h)
Water Inlet temperature (^{o}C)	10 – 20°C
Water flow rate (GPM)	0.05 – 0.1

For most of the conditions in Table 3, CO$_2$ undergoes a transition to pseudo-critical temperature and it is a great care is taken when conducting tests near the pseudo-critical temperature. For example, the specific heat and other thermo-physical properties exhibit a strong nonlinear temperature dependence in the pseudo-critical region and the water flowrate/temperature are adjusted such that the CO$_2$ outlet temperature is at least 0.5 ^{o}C above or below the pseudo-critical temperature.

Heat transfer data reduction and associated uncertainty

The local heat removal for each cooling block is calculated using the measured inlet and outlet water temperatures and the volumetric flowrate of water. Approximately 3" thick insulation layer is wrapped around the test section and the cooling blocks, therefore, the heat loss to the ambient is assumed to be negligible. Water properties are calculated based on the average of the inlet and outlet temperatures, as

the water properties don't vary considerably in the temperature range of interest. For example, for all the experiments performed, the temperature difference between outlet and inlet to the cooling blocks is between 0.5 – 15°C and the temperatures are far away from boiling point. Therefore, assumption of constant properties for water is quite reasonable. The total heat removal rate can be determined from the water side by summing the local heat removal rates from all 20 cooling blocks (10 on the mating plate and 10 on the heat exchanger plate), as shown in Equation (4).

The total heat removal rate can also be alternatively determined from energy balance on the CO_2 side, as shown in Equation (5).

$$\dot{Q}_{H_2O} = \Sigma_1^{20} \dot{V}\rho|_{T_{avg}} C_p|_{T_{avg}} [T_{water,out} - T_{water,in}] \tag{4}$$

$$\dot{Q}_{CO_2} = \dot{m}_{CO_2}(i_{in} - i_{out}) \tag{5}$$

Where, i is the enthalpy (J/kg) and is determined from the measured inlet/outlet temperatures and associated pressures. Inlet and outlet temperatures are measured using platinum RTD with an uncertainty of ±0.15°C. The pressure transducers are calibrated using a deadweight calibrator and the maximum uncertainty is found to be 0.05% of full scale (equivalent to ±1.5 psi). All of these uncertainties are used in the overall energy balance for the CO_2 side. Uncertainty in the measurement of local heat removal rate from the cooling blocks is calculated using Kline and McClintock method, as shown in Equation (6). From Equation (6), the major contributors to the heat removal rate uncertainty are the uncertainty in measurement of water temperature difference and the volumetric flowrate of water.

$$\sigma_{Q_{H_2O}} = \left(\left(\frac{dQ_{H_2O}}{d\dot{V}}\right)^2 \sigma_{\dot{V}}^2 + \left(\frac{dQ_{H_2O}}{d\Delta T}\right)^2 \sigma_{\Delta T}^2\right)^{0.5} \tag{6}$$

All the water flowmeters are connected in series and the cooling water is flown through and collected into a 2000 ml graduated cylinder with an uncertainty of ±20 ml. The frequency output from the flowmeters and the time taken to fill up the cylinder were recorded using Arduino. Following this procedure a calibration curve between the frequency and flowrate was generated for each flowmeter with an overall uncertainty of 1.5% in measurement of volumetric flowrates. In order to reduce the uncertainty of water temperature difference measurements, water outlet thermocouples are calibrated against the inlet thermocouples in-situ by flowing water through each block at temperatures ranging from 10-35°C. The maximum estimated uncertainty in measurement of water temperature difference is ±0.15°C. The overall heat removal rate determined from both water and CO_2 matched well within 10% or less for all the experiments.

Bulk fluid temperature is calculated at ten axial locations. This was accomplished by an energy balance at each subsection (See Figure 4), which consists of cooling block pairs on the mating and the heat exchanger plate. The measured CO_2 inlet pressure and temperature to the test section are used to calculate the specific enthalpy at the inlet (i_{in} or i_1). Assuming a linear pressure drop across the test section, the local bulk enthalpy at the exit of each cooling block sub-section can be determined as shown in Equation (7). The local average enthalpy for each sub-section can then be calculated as in Equation (8).
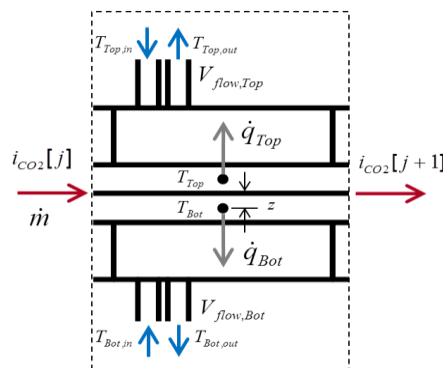

Figure 4: One of the 10-subsections of the heat exchanger showing relevant variables used during data reduction and analysis.

$$i_{j+1} = i_j - \frac{\dot{Q}_{top,j} + \dot{Q}_{bottom,j}}{\dot{m}} \tag{7}$$

$$i = \frac{i_{j+1} + i_j}{2} \tag{8}$$

Finally, the average bulk temperature and any other state-dependent thermo-physical properties can be determined based on the average enthalpy and pressure for each subsection. All the fluid properties are calculated using the NIST REFPROP v9.1 [18].

The wall surface temperature on each plate side is calculated according to a plane-wall conductance equation as shown in Equation (9). The two wall surface temperatures as estimated from the top and bottom of the channels are then averaged and used to determine the local heat transfer coefficient for each sub-section.

$$T_{w,calc}[j] = T_{w,meas}[j] + \frac{Q[j].z[j]}{k_{ss316}A_{cb}}$$

$$T_w[j] = 0.5.(T_{w,calc,top}[j] + T_{w,calc,bottom}[j]) \tag{9}$$

Where, A_{cb} is the cooling block area actively involved in heat transfer (it is estimated to be 1.39" x 2" from an ANSYS Fluent model). An uncertainty of 5% is assumed in the usage of this heat transfer area. All the wall thermocouples are calibrated in-situ with respect to the inlet RTD during isothermal tests (without cooling water flow) and a calibrated uncertainty of ±0.15°C is assumed for uncertainty analysis. The uncertainty associated with the calculation of bulk temperature and wall temperature are estimated using Kline and McClintock method.

From the local heat removal rate, wall temperature, and bulk temperature, the local heat transfer coefficients and Nusselt numbers are calculated from Equations (10)-(12).

$$htc[j] = \frac{Q_{top}[j] + Q_{bottom}[j]}{A_s.(T_b[j] - T_w[j])} \tag{10}$$

$$Nu[j] = \frac{htc[j].D_h}{k_b} \tag{12}$$

Uncertainty in the measurement of local heat transfer coefficient and Nusselt numbers are calculated using Equations (13)-(14).

$$\sigma_{htc}[i] = \left(\left(\frac{dhtc}{dQ}[i] \right)^2 \sigma_Q[i]^2 + \left(\frac{dhtc}{dA_s}[i] \right)^2 \sigma_{A_s}^2 + \left(\frac{dhtc}{dT_b}[i] \right)^2 \sigma_{T_b}[i]^2 + \left(\frac{dhtc}{dT_w}[i] \right)^2 \sigma_{T_w}[i]^2 \right)^{0.5} \tag{13}$$

$$\sigma_{Nu}[i] = \left(\left(\frac{dNu}{dhtc}[i] \right)^2 \sigma_{htc}[i]^2 + \left(\frac{dNu}{dD_h}[i] \right)^2 \sigma_{D_h}^2 + \left(\frac{dNu}{dk_b}[i] \right)^2 \sigma_{k_b}[i]^2 \right)^{0.5} \tag{14}$$

Average heat transfer coefficient and Nusselt number for each experiment are calculated using Equations (15)-(16).

$$\overline{htc} = \frac{0.5(\dot{Q}_{CO_2} + \dot{Q}_{H_2O})}{N.A_s(\overline{T}_b - \overline{T}_w)} \tag{15}$$

$$\overline{Nu} = \overline{htc}.\frac{D_h}{\overline{k_b}} \tag{16}$$

Pressure data reduction and associated uncertainty

The total pressure drop measured across the heat exchanger test section is comprised of four components as shown in Equation (17).

$$\Delta P_{measured} = \Delta P_{friction} + \Delta P_{local} + \Delta P_{accel} + \Delta P_{gravity} \qquad (17)$$

Where,

$$\Delta P_{friction} = f \frac{L}{D_h} \frac{G^2}{2\overline{\rho}}$$

$$\Delta P_{accel} = G^2 \left(\frac{1}{\rho_{out}} - \frac{1}{\rho_{in}} \right)$$

$$\Delta P_{gravity} = \pm g \left(\frac{i_{out}\rho_{out} + i_{in}\rho_{in}}{i_{out} + i_{in}} \right) L\sin\theta$$

All the experiments for this work were performed in horizontal configuration, which eliminates the pressure drop component due to gravity. The acceleration pressure losses due to density changes over the length are computed from the measured mass flowrate and the inlet and outlet conditions. The local pressure drop arises from the fluid contraction at the inlet, due to the mixing manifold splitting the flow to each channel, and expansion from the channels to the manifold at the outlet. Expansion and contraction pressure losses are well known from published values, so the local pressure losses can be determined by the following equations:

$$\Delta P_{local} = \Delta P_{expansion} + \Delta P_{contraction} \qquad (18)$$

$$\Delta P_{expansion} = \left[1 - \frac{A_c}{A_{manifold}} \right]^2 \rho_{out} \frac{v_{out}^2}{2}$$

$$\Delta P_{contraction} = 0.5 \left[1 - \frac{A_c}{A_{manifold}} \right]^{0.75} \rho_{in} \frac{v_{in}^2}{2}$$

Where, A_c is the cross-sectional area of the fins and $A_{manifold}$ is the cross-sectional area of the manifolds. Using this procedure, the pressure drop due to friction can be extracted from the measured pressure drop from the experiments.

RESULTS AND DISCUSSION

Heat transfer and pressure data was collected and reduced as described in the previous section, with experimental average heat transfer coefficient and Nusselt number shown in Figure 5 plotted versus the average bulk temperature for the Offset NACA0020 Airfoil fin heat exchanger plate.
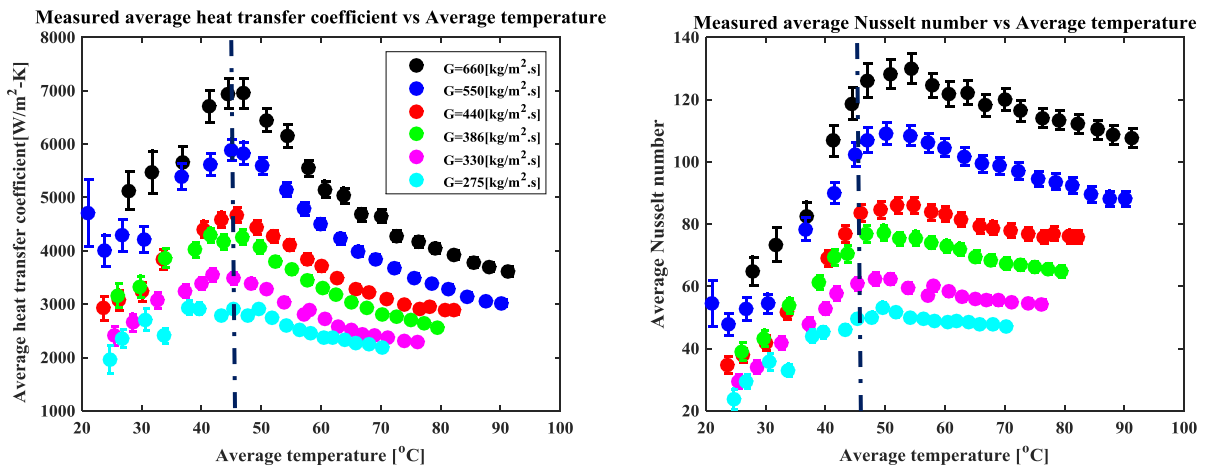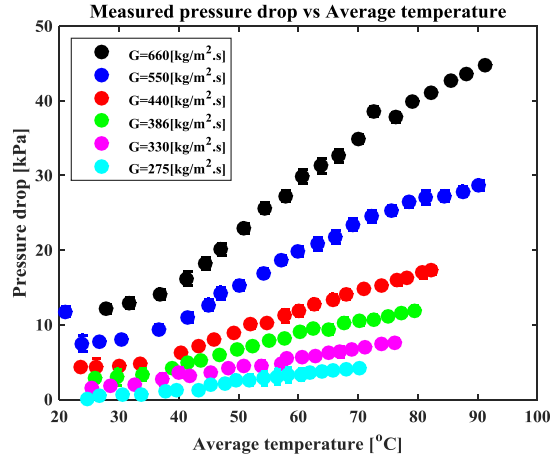

Figure 5: Measured Average heat transfer coefficient and Nusselt number plotted as a function of

the Average bulk temperature for the Offset NACA0020 Airfoil fin heat exchanger plate. The inlet pressure is set to 10.2 MPa for all the data points.

Each data point in Figure 5 is based on an average of 500 data points taken at rate of 1 Hz. It can be seen that the heat transfer is enhanced near the pseudo-critical temperature (~46°C for 10.2 MPa, marked as dashed vertical line in Figure 5). This is mainly due to the increased specific heat in the pseudo-critical region rather than enhancement of heat transfer due to increase in heat transfer area or other geometrical features. Mean uncertainty in measurement of average heat transfer coefficient and Nusselt number is less than 5%. The maximum uncertainty is ~20% near the pseudo-critical temperature for operating pressure of 7.5 MPa.

Figure 6: Measured pressure drop plotted as a function of the Average bulk temperature for the Offset NACA0020 Airfoil fin heat exchanger plate. The inlet pressure is set to 10.2 MPa for all the data points.

Figure 6 presents the pressure drop data for the Offset NACA0020 Airfoil fin heat exchanger plate measured directly. Uncertainty bars in Figure 6 represent the combined propagated uncertainty of both the instrument uncertainty and the measurement deviation from average values. For temperatures greater than the pseudo-critical temperature density of the fluid resembles that of a gas and the frictional pressure drop is high in this region due to increased flow velocities. As the temperatures falls below the pseudo-critical temperature a steep decrease in the frictional pressure gradient is noticed for all the mass fluxes. This is because the density increases rapidly as the temperature falls below the pseudo-critical temperature.

For data presented in Figure 5 and 6, the average temperature is calculated by taking into account the non-linear temperature variation along the length of the heat exchanger. Figure 7 presents an example of measured wall temperature profile along the length of heat exchanger plate along with the calculated bulk temperature profile via measured local cooling rates. The temperature profiles clearly exhibit a non-linear variation along the length and the average bulk as well as wall temperatures are calculated by using integral method as shown in Equations (19)-(20).

$$\overline{T_b} = \frac{1}{L}\int_0^L T_b(x).dx \qquad (19)$$

$$\overline{T_w} = \frac{1}{L}\int_0^L T_w(x).dx \qquad (20)$$

Since the thermo-physical properties exhibit a non-linear behavior with respect to temperature, the average properties along the heat exchanger are calculated as defined by set of Equations (21).

$$\bar{\rho} = \frac{1}{L}\int_0^L \rho(T).dx \; ; \; \bar{\mu} = \frac{1}{L}\int_0^L \mu(T).dx \; ; \; \overline{Pr} = \frac{1}{L}\int_0^L Pr(T).dx$$

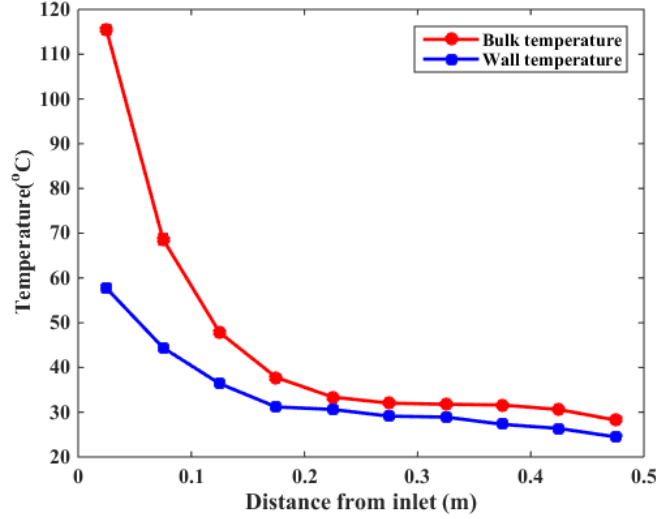$$\overline{Re} = G.D_h/\bar{\mu} \tag{21}$$

Figure 7: Measured wall temperature profile and calculated bulk temperature profile (via measured local cooling rate) as a function of the heat exchanger length for one of the experimental case.

Derivation of friction factor correlation

Frictional pressure drop for each of the experimental runs can be calculated as,

$$\Delta P_{calc} = \sum_{i=1}^{N} 2\left(\frac{L}{N.D_h}\right)\frac{G^2}{\rho_i}f_i \tag{22}$$

Where, ρ_i and f_i represent the calculated local density and friction factor. Assuming a friction factor of the form,

$$f_i = aRe_i^b$$

The coefficients a and b were found out by following least-squares curve fitting of the form,

$$\sum_{i=1}^{N_{expt}}\left(\Delta P_{calc}^i - \Delta P_{exp}^i\right) \rightarrow minimum$$

Table 4 summarizes the coefficients a, b determined for both the tested heat exchanger plates.

Table 4: Coefficients a, b determined from fitting the fanning friction factor, aRe^b to the experimental data for both the heat exchanger plates.

Heat exchanger plate	a	b
Offset rectangular fin plate	0.0276	-0.002
Offset NACA0020 airfoil fin plate	0.0077	0.1201

Figure 8 and 9 presents the predictions from fitted friction factor correlation to the experimentally measured values for Offset rectangular and NACA0020 airfoil fin plates respectively. The proposed correlations can predict the frictional pressure drop with the mean average deviation error of 11.2% and the standard deviation error of 13.7% for the Offset rectangular fin HEX plate. 80% of the experimental data is predicted within ±15% and 91.7% of the experimental data is predicted within ±25%. For the offset NACA0020 airfoil fin HEX plate the mean average deviation error is 8.1% and the standard deviation error of 11%. 88.6% of the experimental data is predicted within ±15% and 94.7% of the experimental data is predicted within ±25%.
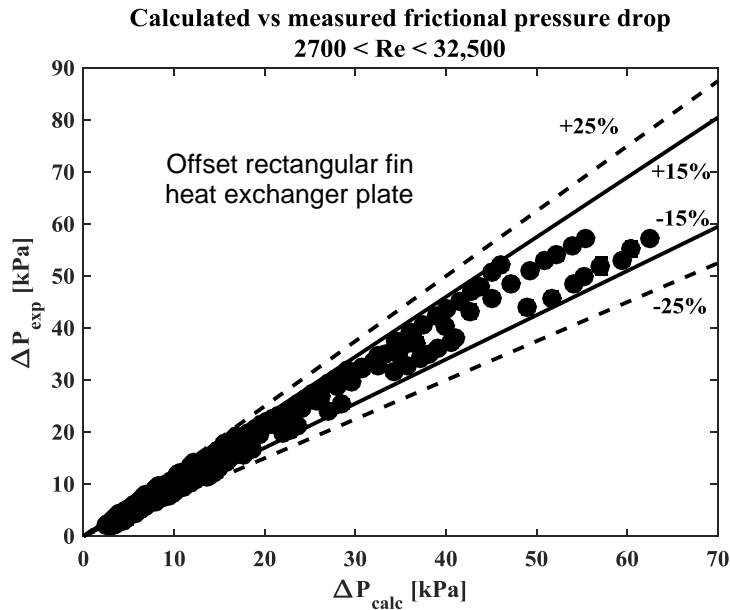

Figure 8: Experimental vs. calculated frictional pressure drop for Offset rectangular fin HEX plate.
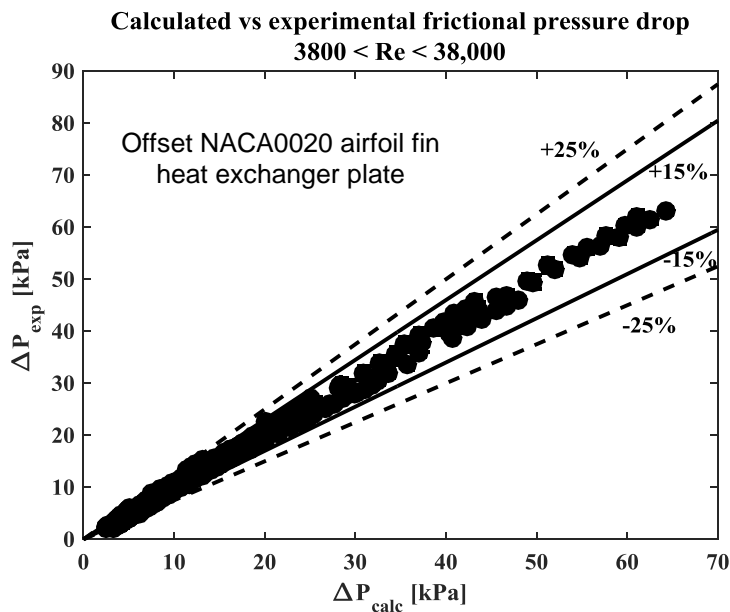

Figure 9: Experimental vs. calculated frictional pressure drop for Offset NACA0020 airfoil fin HEX plate.

Derivation of Nusselt number correlation

Average Nusselt number (Nu_{exp}) for each of the experimental run is calculated as described in the previous sections. The calculated Nusselt number is assumed of the form,

$$Nu_{calc} = a\overline{Re}^b\overline{Pr}^c \left(\frac{\overline{\rho_b}}{\rho_w}\right)^d \left(\frac{\overline{C_{pb}}}{\overline{C_p}}\right)^e \tag{23}$$

Where, $\overline{C_p} = \frac{\overline{i_w}-\overline{i_b}}{\overline{T_w}-\overline{T_b}}$ and other average properties are calculated as described in Equation (21). A close look at Equation (23) shows that it of the form $a\overline{Re}^b\overline{Pr}^c$ with additional wall to bulk property ratios to take into account non-linear variation of thermo-physical properties with temperature.

The coefficients a through e were found out by following least-squares curve fitting of the form,

$$\sum_{i=1}^{N_{expt}}\left(Nu^i_{calc} - Nu^i_{exp}\right) \to minimum$$

Table 5 summarizes the coefficients a through e determined for both the tested heat exchanger plates.

Table 5: Coefficients a, b determined from fitting the fanning friction factor, aRe^b to the experimental data for both the heat exchanger plates.

Heat exchanger plate	a	b	c	d	e
Offset rectangular fin plate	0.1034	0.7054	0.3489	0.9302	-0.3660
Offset NACA0020 airfoil fin plate	0.0601	0.7326	0.3453	0.4239	-0.3556

Figure 10 and 11 presents the predictions from fitted Nusselt number correlation to the experimentally measured values for Offset rectangular and NACA0020 airfoil fin plates respectively.
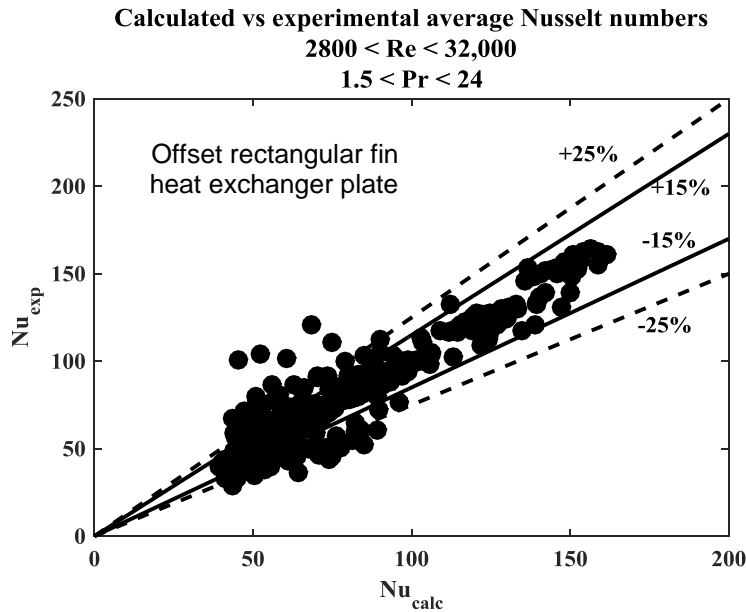

Figure 10: Experimental vs. calculated Nusselt numbers for Offset rectangular fin HEX plate.
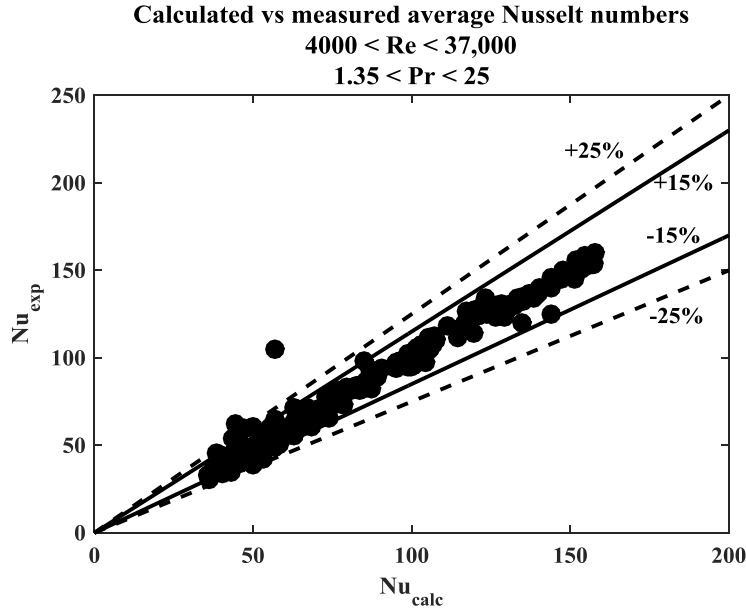
Figure 11: Experimental vs. calculated Nusselt numbers for Offset NACA0020 airfoil fin HEX plate.

The proposed correlations can predict the experimental Nusselt numbers with the mean average deviation error of 9.1% and the standard deviation error of 15.4% for the Offset rectangular fin HEX plate. 90% of the experimental data is predicted within ±15% and 93% of the experimental data is predicted within ±25%. For the offset NACA0020 airfoil fin HEX plate the mean average deviation error is 5.2% and the standard deviation error of 8%. 96% of the experimental data is predicted within ±15% and 99% of the experimental data is predicted within ±25%.

Extension of Nusselt number correlation to gas-like regimes

Based on the variation in thermophysical properties, the supercritical heat transfer and pressure drop data can be divided into three regimes, liquid-like, pseudo-critical transition, and gas-like. These flow regime transition criteria are defined quantitatively based on the specific work of thermal expansion/contraction, E_o, by Kurganov *et al.* as follows:

$$E_o = P.\beta/(\rho C_p)$$

E_o is the ratio of the work done by the fluid during cooling to the heat convected out of it during the flow. Figure 12 shows the plot of E_o with respect to temperature and enthalpy for carbon dioxide for three different operating pressures (same as the collected data) in the critical region. The plot of E_o versus enthalpy shows a gradual increase to a point where $E_o = 0.05$, followed by an abrupt change in the slope until $E_o \sim 0.23 - 0.24$ where the curve reaches a maximum and then decrease with further increase in enthalpy. Based on this, three regimes are defined: (a) a liquid-like (low temperature) regime where the change in E_o with temperature/enthalpy is gradual mostly due to small property variation; For each pressure, temperature where the abrupt change in slope of E_o v/s T occurs is determined. (b) Pseudo-critical transition regime where the change in E_o is rapid with temperature; and (c) the gas-like regime where the E_o starts to decline as temperature increases. The transition from the pseudo-critical transition regime to the gas like were found when $dEo/dT = 0$. Table 6 shows the corresponding temperature ranges for three different flow regimes described above and Equation (24) presents the temperature as a function of temperature at which transition to a gas like phase occurs.
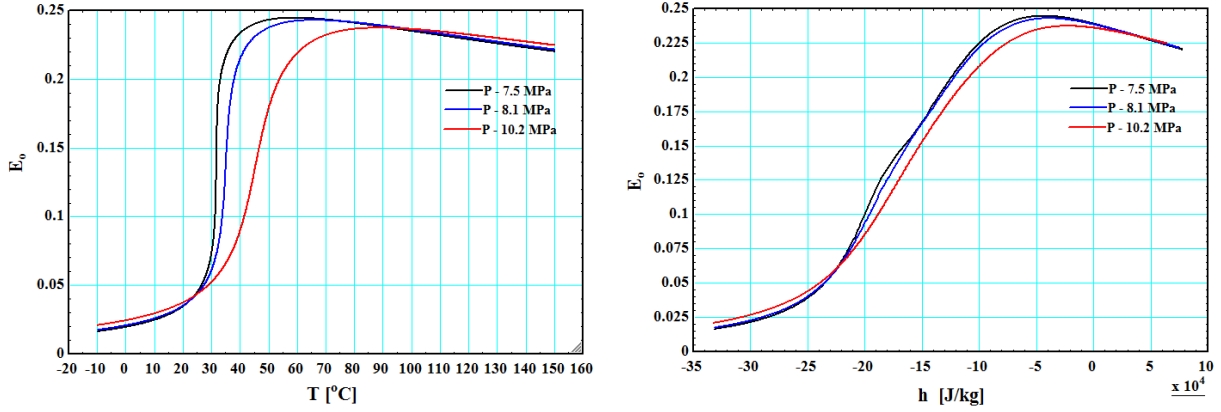
Figure 12: Plot of E_o versus temperature and enthalpy for carbon dioxide in the critical region.

Table 6: Boundaries determined for the three flow regimes

Pressure [MPa]	Liquid-like regime	Pseudo-critical transition regime	Gas-like regime
7.5	T < 26.46°C	26.46°C ≤ T ≤ 58.79°C	T > 58.79°C
8.1	T < 27.25°C	27.25°C ≤ T ≤ 65.76°C	T > 65.76°C
10.2	T < 28.82°C	28.82°C ≤ T ≤ 88.44°C	T > 88.44°C

$$T_{GL} = 0.0034P^3 - 0.3284P^2 + 15.963P - 43.85 \qquad (24)$$

Where, T_{GL} is in °C and P is in MPa.

The Nusselt number correlations presented in Equation (23) and Table 5 can be extended to a gas like regime by dropping the property ratio terms since the thermo-physical properties variation is not as drastic as near the pseudo-critical region.
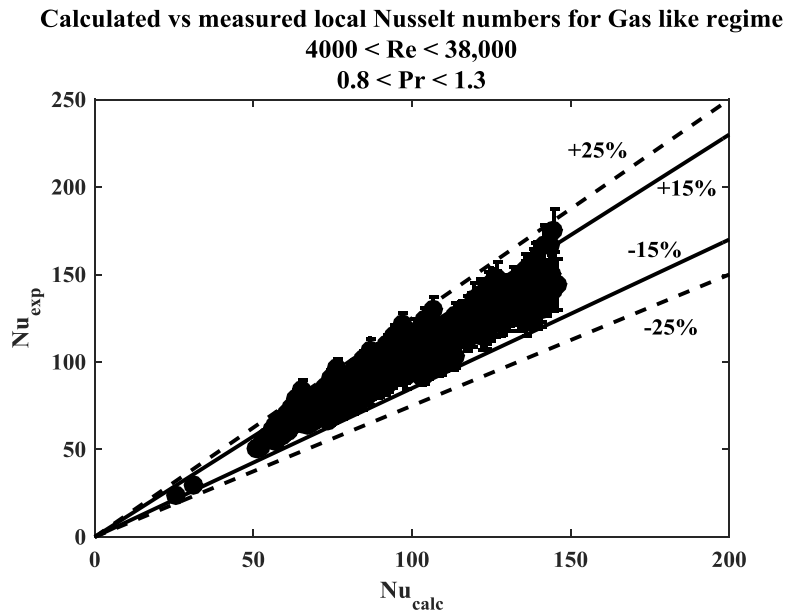

Figure 13: Experimental vs. calculated Nusselt numbers for Offset NACA0020 airfoil fin HEX plate by extending the proposed correlation to gas-like regime and dropping the property ratio terms.

For example, the Nusselt numbers of Offset NACA0020 airfoil fin HEX plate can be calculated using the following relationship by dropping the property terms in Equation (23),

$$Nu_{calc} = 0.0601 Re^{0.7326} Pr^{0.3453} \qquad (25)$$

The correlation proposed in Equation (25) is screened against the measured local Nusselt numbers for $T_b > T_{GL}$ (Bulk temperature greater than gas-like transition temperature). Figure 13 presents the comparison between experimentally measured gas-like Nusselt numbers and calculated values using Equation (25). The proposed correlation can predict the experimental Nusselt numbers with the mean average deviation error of 5.6% and the standard deviation error of 6.9%. 98% of the experimental data is predicted within ±10% and 100% of the experimental data is predicted within ±15%.

Comparison of the thermal-hydraulic performance with existing correlations

In this section, the thermal-hydraulic performance of the offset rectangular and NACA0020 airfoil HEX plates are compared to that of the existing correlations for other printed circuit heat exchanger geometries. Ngo et al. [7] proposed friction factor and Nusselt number correlations for the discontinuous S-shaped fin and zig-zag channel PCHEs as shown in Equation (26) and (27) respectively.

$$f_{SS} = 0.4545 Re^{0.43}; Nu_{SS} = 0.174 Re^{0.593} Pr^{0.43} \qquad (26)$$

$$f_{ZZ} = 0.1924 Re^{-0.091}; Nu_{ZZ} = 0.629 Re^{0.629} Pr^{0.317} \qquad (27)$$

These correlations along with the correlations proposed in the current study are plotted as a function of Reynolds number as shown in Figure 14. As can be seen both the Offset rectangular and NACA0020 airfoil fins offer significantly lower pressure drop factor when compared to the zig-zag channels but slightly higher than the S-shaped fins in turbulent flow regime. However, the Nusselt numbers of both Offset rectangular and NACA0020 airfoil fins are significantly higher than S-shaped fins and almost comparable to that of zig-zag channel PCHE.
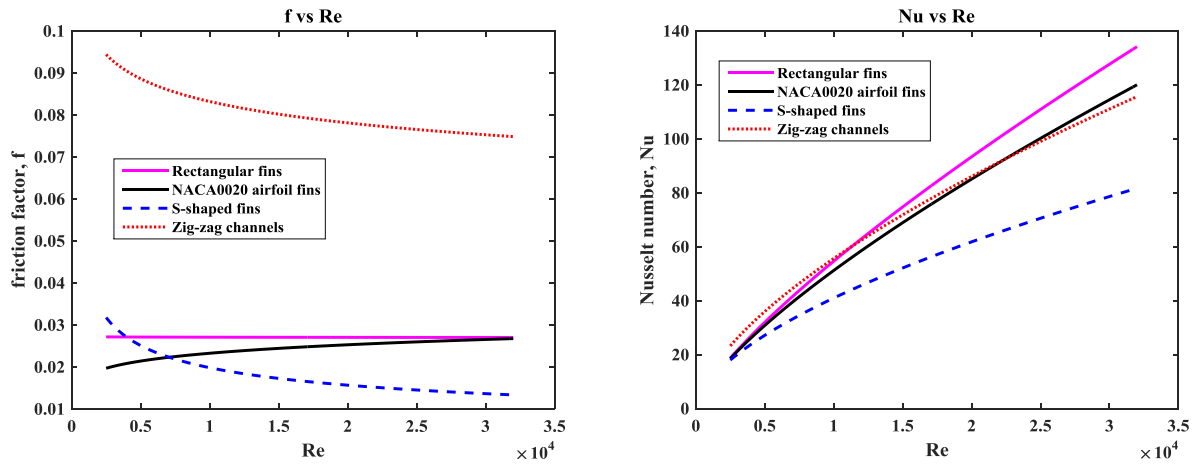

Figure 14: Comparison of variation of fanning friction factor and Nusselt number with Reynolds number for different PCHE surface patterns.

CONCLUSIONS

Heat transfer and pressure drop characteristics of flow of supercritical carbon dioxide through discontinuous Offset rectangular and NACA0020 airfoil fin geometries was investigated experimentally.

Both the heat exchanger geometries exhibited similar Nusselt numbers and pressure drop characteristics. Average and local Nusselt number correlations as well as fanning friction factor correlations are proposed based on the least squares fitting to the experimental data. The pressure drop offered by these heat exchanger plates is significantly lower than that of zig-zag channel PCHE from literature with nearly similar heat transfer performance.

REFERENCES

[1] Ishizuka, Takao. "Thermal-Hydraulic Characteristics of a Printed Circuit Heat Exchanger in a Supercritical CO_2 Loop." In *The 11th International Topical Meeting on Nuclear Reactor Thermal-Hydraulics, 2005*. 2005.

[2] Nikitin, Konstantin, Yasuyoshi Kato, and Lam Ngo. "Printed circuit heat exchanger thermal–hydraulic performance in supercritical CO 2 experimental loop." *International Journal of Refrigeration* 29, no. 5 (2006): 807-814.

[3] Tsuzuki, Nobuyoshi, Yasuyoshi Kato, and Takao Ishiduka. "High performance printed circuit heat exchanger." *Applied Thermal Engineering* 27, no. 10 (2007): 1702-1707.

[4] Yasuyoshi Kato. "How New Microchannel Heat Exchanger Reduced Pressure Drop to 1/6 Inheriting High Heat Transfer Performance." Supercritical CO_2 Power Cycle Symposium (2011)

[5] Ngo, Tri Lam, Yasuyoshi Kato, Konstantin Nikitin, and Nobuyoshi Tsuzuki. "New printed circuit heat exchanger with S-shaped fins for hot water supplier." *Experimental Thermal and Fluid Science* 30, no. 8 (2006): 811-819.

[6] Nikitin, Konstantin, Yasuyoshi Kato, and Takao Ishizuka. "Experimental thermal-hydraulics comparison of microchannel heat exchangers with zigzag channels and S-shaped fins for gas turbine reactors." (2007).

[7] Ngo, Tri Lam, Yasuyoshi Kato, Konstantin Nikitin, and Takao Ishizuka. "Heat transfer and pressure drop correlations of microchannel heat exchangers with S-shaped and zigzag fins for carbon dioxide cycles." *Experimental Thermal and Fluid Science* 32, no. 2 (2007): 560-570.

[8] Moisseytsev, A., J. J. Sienicki, D. H. Cho, and M. R. Thomasa. "Comparison of heat exchanger modeling with data from CO_2-to-CO_2 printed circuit heat exchanger performance tests." In *Proceedings of the 2010 International Congress on Advances in Nuclear Power Plants-ICAPP'10*. 2010.

[9] Southall, David, Renaud Le Pierres, and Stephen John Dewson. "Design considerations for compact heat exchangers." In *Proceedings of ICAPP*, vol. 8, pp. 8-12. 2008.

[10] Kim, In Hun, Hee Cheon No, Jeong Ik Lee, and Byong Guk Jeon. "Thermal hydraulic performance analysis of the printed circuit heat exchanger using a helium test facility and CFD simulations." *Nuclear Engineering and Design* 239, no. 11 (2009): 2399-2408.

[11] Kim, In Hun, and Hee Cheon No. "Thermal hydraulic performance analysis of a printed circuit heat exchanger using a helium–water test loop and numerical simulations." *Applied Thermal Engineering* 31, no. 17 (2011): 4064-4073.

[12] Kim, In Hun, and Hee Cheon No. "Thermal–hydraulic physical models for a Printed Circuit Heat Exchanger covering Helium, He–CO_2 mixture, and water fluids using experimental data and CFD." *Experimental Thermal and Fluid Science* 48 (2013): 213-221.

[13] Mylavarapu, Sai K. *Design, fabrication, performance testing, and modeling of diffusion bonded compact heat exchangers in a high-temperature helium test facility*. The Ohio State University, 2011.

[14] Kruizenga, Alan Michael. *Heat transfer and pressure drop measurements in prototypic heat exchanges*

for the supercritical carbon dioxide Brayton power cycles. 2010.

[15] Carlson, Matthew D. "Measurement and Analysis of the Thermal Hydraulic Performance of Several Printed Circuit Heat Exchanger Channel Geometries.", University of Wisconsin--Madison, 2012.

[16] Kim, Dong Eok, Moo Hwan Kim, Jae Eun Cha, and Seong O. Kim. "Numerical investigation on thermal–hydraulic performance of new printed circuit heat exchanger model." *Nuclear Engineering and Design* 238, no. 12 (2008): 3269-3276.

[17] Pidaparti, Sandeep R., Jacob A. McFarland, Mark M. Mikhaeil, Mark H. Anderson, and Devesh Ranjan. "Investigation of Buoyancy Effects on Heat Transfer Characteristics of Supercritical Carbon Dioxide in Heating Mode." *Journal of Nuclear Engineering and Radiation Science* 1, no. 3 (2015): 031001.

[18] Lemmon, Eric W., Marcia L. Huber, and Mark O. McLinden. "NIST reference fluid thermodynamic and transport properties–REFPROP." (2002).

ACKNOWLEDGEMENTS